PROCEEDINGS A

royalsocietypublishing.org/journal/rspa

Research

Cite this article: Zeng W, Dai Z, Wei Y. 2026 Adhesion of elastic membranes. Part I: a generalized Tabor parameter. *Proc. R. Soc. A* **482**: 20250932.
https://doi.org/10.1098/rspa.2025.0932

Received: 28 October 2025
Accepted: 24 November 2025

Subject Areas:
mechanics

Keywords:
elastic membrane, adhesion, van der Waals forces, pull-off force, Tabor parameter

Authors for correspondence:
Zhaohe Dai
e-mail: daizh@pku.edu.cn
Yueguang Wei
e-mail: weiyg@pku.edu.cn

Adhesion of elastic membranes. Part I: a generalized Tabor parameter

Weijia Zeng, Zhaohe Dai and Yueguang Wei

School of Mechanics and Engineering Science, State Key Laboratory for Turbulence and Complex Systems, Peking University, Beijing 100871, People's Republic of China

WZ, 0009-0009-3127-6564; ZD, 0000-0002-5205-089X

For elastic slabs, adhesive behaviour is often described by continuum theories such as Johnson–Kendall–Roberts (JKR) for compliant systems and by atomistic force-based models such as Derjaguin–Muller–Toporov (DMT) for rigid systems, with the transition between them typically characterized by the Tabor parameter. In contrast, the adhesion mechanics of thin elastic membranes remain less understood. Particularly, although recent studies have applied the JKR framework to membranes, the corresponding transition towards the rigid limit has not been fully established. A central difficulty lies in the fact that the effective rigidity of a membrane is influenced not only by its intrinsic Young's modulus but also by in-plane residual tension and out-of-plane loading such as pressure. Here, we address this issue by introducing a membrane-specific Tabor parameter that incorporates all of these factors. This parameter is validated through numerical calculations and previous experimental measurements, providing a consistent framework to classify membrane adhesion across diverse systems, from biological membranes to microelectromechanical devices.

1. Introduction

Adhesion is a ubiquitous surface phenomenon in nature and engineering [1], governing processes that range from biological attachment and tissue interactions [2,3] to the operation of small-scale devices and flexible electronics [4,5]. To describe adhesion, a variety of theoretical models have been established. Probably the first quantitative model of adhesion was proposed by

THE ROYAL SOCIETY
PUBLISHING

Bradley [6], who considered long-range intermolecular forces and showed that the pull-off force between two rigid spheres of effective radius R_s is $2\pi\gamma R_s$, where γ is the adhesion energy density, that is, the energy per unit area required to separate two surfaces from equilibrium to infinity. For relatively deformable spheres, the Johnson–Kendall–Roberts (JKR) theory introduced an energetic argument to demonstrate an elasticity-independent pull-off force of $\frac{3}{2}\pi\gamma R_s$ [7]. By contrast, the Derjaguin–Muller–Toporov (DMT) model [8], which also considers elastic deformation but neglects additional deformation induced by interfacial forces, recovers Bradley's result in the limit of rigid spheres. The discrepancies among these models were rationalized by the *Tabor parameter* [9], which characterizes the transition from the JKR limit for compliant contacts to the Bradley/DMT limit for rigid contacts. Subsequent refinements, such as the Maugis–Dugdale [10] and Greenwood models [11], yielded an adhesion map that delineates the regimes of validity for different theories [12]. Despite these classical advances, efforts continue to enrich adhesion models by incorporating new physical ingredients—including capillarity [13–15], viscoelasticity [16,17], vibration [18,19], lubrication dynamics [20], surface tension and stresses [21–24] and heterostructures [25]. These efforts were largely driven by applications involving materials with diverse mechanical responses and complex operating environments.

Among the new ingredients, a particularly important one arises from thin geometry [26–28]. On one hand, when one of the contacting bodies is thin, its effective compliance is determined not only by material properties but also by external loading conditions and by where and how its boundaries are constrained [29,30]. For example, atomically thin graphene sheets suspended over a trench or a hole are approximately clamped at the edges (see figure 1a) [33]. In this configuration, transverse pressure can induce in-plane strain proportional to the square of the pressurized deflection, thereby stiffening the response to indentation contact [34–36]. On the other hand, adhesion—as a surface phenomenon sensitive to the surface-to-volume ratio of solids—is strongly amplified in thin geometries [37,38]. This can be evidenced by the nearly inevitable pull-off forces observed in indentation tests on thin membranes across scales, from macroscopic adhesive tapes to nanoscale graphene (see figure 1b) [39–41]. Consequently, the interplay between these rich mechanical responses and the strong adhesion effect gives rise to considerable complexity. A concrete illustration can be provided by slightly pressurized graphene sheets, which exhibit not only a stiffer indentation response but also a markedly larger pull-off force due to this interplay (figure 1c) [32], a phenomenon described as 'stiffer is stickier' in [31].

The pull-off force for membranes in the rigid limit remains consistent with Bradley's prediction, $2\pi\gamma R_s$. In contrast, in the compliant limit, it has recently been shown to reduce to $\pi\gamma R_s$ [42,43], a value slightly different from the JKR result for elastic slabs but, remarkably, independent of both the size and the constitutive behaviour of the membrane [44]. Hence, the stiffer is stickier phenomenon observed in thin membranes is conceptually analogous to the transition from JKR to Bradley in elastic slabs as their Young's modulus increases and the Tabor parameter decreases [31]. Defining a Tabor parameter for elastic membranes, however, is non-trivial, since membranes may appear stiff either owing to their intrinsically large in-plane modulus or as a consequence of pretension or external pressurization. Previous efforts have typically focused on a single stiffening mechanism, such as pressurization [31], or on simplified systems, such as linearized membrane theory [45–47]. Despite the coexistence of multiple stiffening sources and the intrinsic nonlinearity of the problem, to date, a unified framework that captures how these different sources of stiffening collectively govern the adhesion of elastic membranes remains elusive.

This work aims to address this gap in thin membrane adhesion by elucidating how the elastic modulus, pretension, pressure and membrane geometry together control the transition of the pull-off force from the microscopic (Bradley) limit to the macroscopic (JKR-type) limit. To this end, we propose a membrane-specific generalization of the Tabor parameter, which shows excellent agreement with both numerical simulations and experimental measurements. The remainder of this paper is organized as follows. In §2, we outline the adhesion problem of elastic membranes and introduce both macroscopic and microscopic perspectives. In §3, we develop develops the macroscopic model, including a discussion of a combined vertical characteristic length scale. In §4, we present the microscopic model and identify three routes through which a membrane can

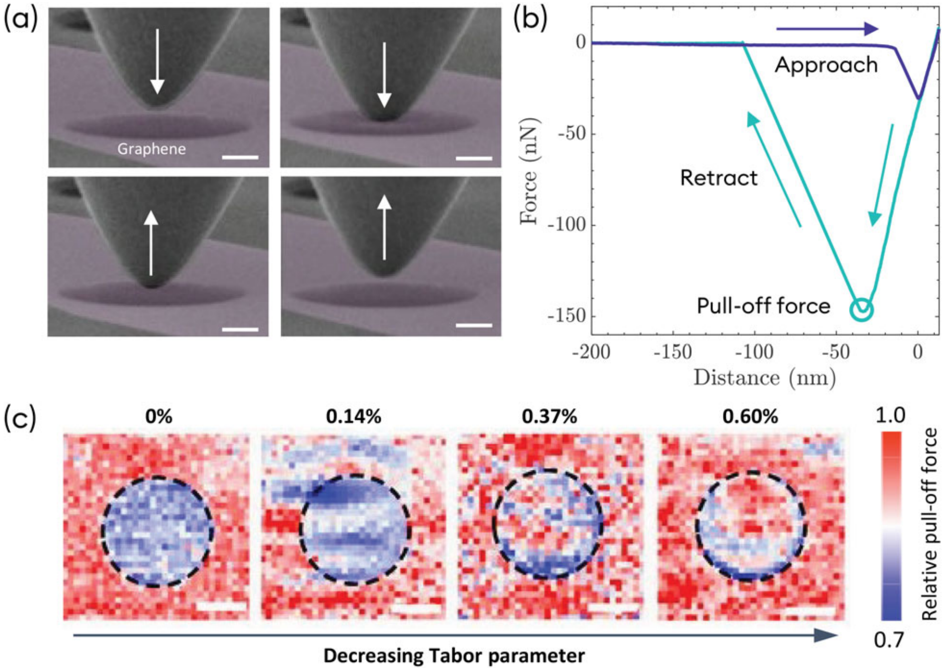

Figure 1. Phenomenology. (a) *In situ* scanning electron microscope images showing an indenter approaching and retracting from a suspended, slightly pressurized monolayer graphene sheet. Scale bars: 1 μm. (b) Force–displacement curves from the indentation experiment. The purple curve corresponds to the approaching process, during which the indenter suddenly jumps into contact with the graphene sheet, while the green curve corresponds to the retracting process, where the indenter abruptly detaches after reaching a critical pulling force (i.e. the pull-off force). Note that the results in (a,b) are measured from a different specimen but obtained using the same experimental set-up reported in [31]. (c) Relative pull-off force maps measured on graphene suspended over a circular hole. The pull-off forces are normalized by the average values measured on the supported region. From left to right, the graphene is increasingly pressurized, with the induced biaxial strain at the centre of the hole indicated (up to 0.6%). Scale bars: 2 μm. Figures in (c) are reproduced from [32] with permission.

effectively behave as rigid, leading to three subparameters and a unified, generalized parameter. In §5, we demonstrate how this generalized Tabor parameter can be applied to interpret previous pull-off force measurements on elastic membranes. Finally, in §6, we summarize our findings and discuss their broader implications for adhesion in thin membranes.

2. Problem statement

Figure 2 illustrates the system under study: a rigid sphere of radius R_s interacting with a thin elastic membrane of radius R_f. The membrane is clamped under a pretension T_{pre} and subjected to a moderate transverse pressure p. Its in-plane elastic properties are characterized by Poisson's ratio ν and in-plane stiffness Et, where E and t denote the Young's modulus and thickness of the membrane, respectively. Following the experimental configuration shown in figure 1, we consider a push–pull process. During the pushing stage, the sphere approaches the membrane and establishes adhesive contact; during the pulling stage, it retracts. Since our primary interest lies in the pull-off force, we define the upward pulling direction as positive, such that a positive force is required to detach the sphere from the membrane.

Analogous to the classical adhesion mechanics of elastic slabs, membrane adhesion can be analysed from two perspectives. From the macroscopic perspective (figure 2b), the membrane is divided into a contact zone of area A_{contact} and radius a, and a non-contact zone for $r > a$.

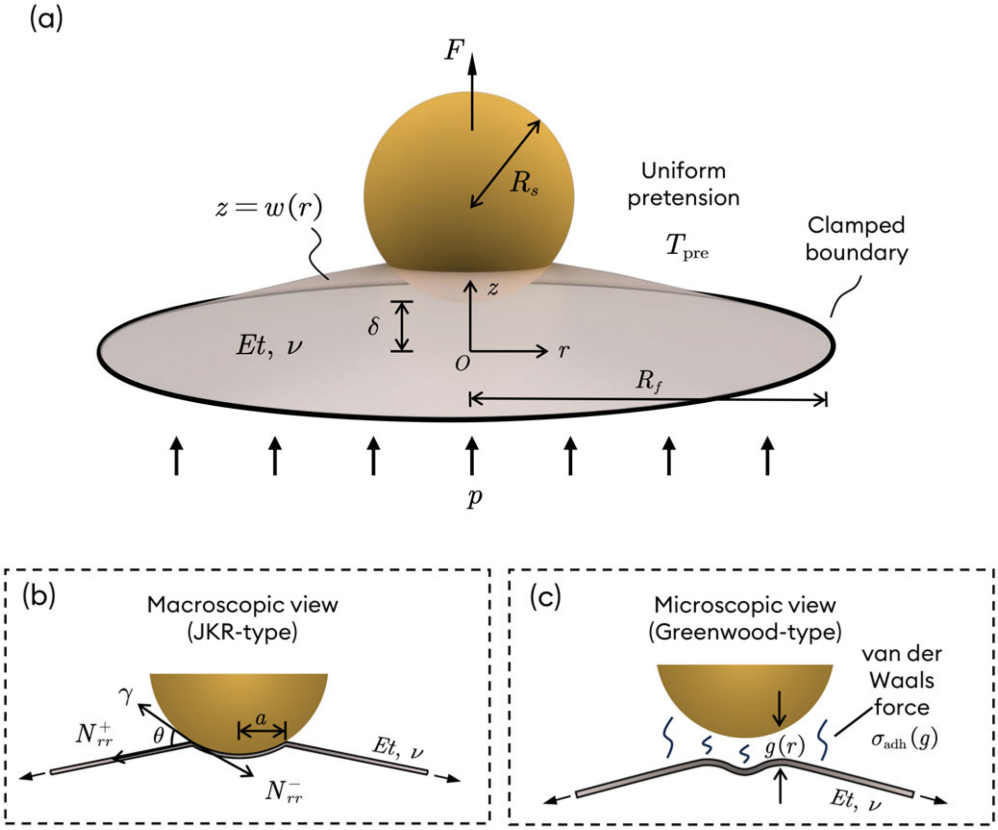

Figure 2. Problem description. (a) Schematic of a rigid sphere in adhesive contact with a clamped elastic membrane subjected to a uniform pretension, showing the key physical quantities. Owing to the presence of adhesion, a finite pulling force is required to separate the sphere from the membrane. (b) Macroscopic view of the adhesion. The membrane is divided by the contact line at $r = a$ into a contact zone ($r < a$) and a non-contact zone ($r > a$). In the presence of adhesion γ, a slope discontinuity is expected at the contact line, which can be described by Young's equation given in equation (3.8). (c) Microscopic view of the adhesion. There is no distinct contact zone; adhesion arises from long-range intermolecular (van der Waals) forces acting across the interface with magnitude depending on the local interface separation g.

Formation of the contact zone reduces the surface energy, $\gamma A_{\text{contact}}$, with γ the adhesion energy density, which is balanced by the additional elastic deformation energy of the membrane. Consequently, the contact radius is determined by minimizing the total energy of the system, which includes the elastic energy, the work done by the applied force and the adhesion energy, i.e.

$$\mathcal{U}_{\text{tot}} = U_{\text{elastic}} - F\delta - \gamma A_{\text{contact}}, \tag{2.1}$$

where F and δ denote the pulling force and displacement, respectively. The equilibrium contact area is then obtained from

$$\left.\frac{\partial \mathcal{U}_{\text{tot}}}{\partial A_{\text{contact}}}\right|_{F \text{ or } \delta} = 0. \tag{2.2}$$

It is therefore natural to refer to this framework as JKR-type adhesion.

From the microscopic perspective, by contrast, adhesion originates from intermolecular forces acting across the interface, a framework we refer to as Greenwood-type adhesion [11]. For a membrane interacting with a rigid sphere, the local adhesive traction can be modelled using a simplified Lennard–Jones (LJ)-type potential [48–50], given by

$$\sigma_{\text{adh}}(g) = \frac{8\gamma}{3z_0}\left[\left(\frac{z_0}{g}\right)^3 - \left(\frac{z_0}{g}\right)^9\right], \tag{2.3}$$

where $g(r)$ is the local separation distance between the surfaces and z_0 is the equilibrium spacing. Integrating this traction over the contact area provides the total adhesive force at the microscopic level. In the following, we develop both the macroscopic (JKR-type) and microscopic (Greenwood-type) adhesion models and aim to integrate them into a unified multiscale description, which can capture the effects of membrane elasticity, pretension, pressure and geometry on the pull-off behaviour.

3. The macroscopic adhesion model

(a) The mixed boundary value problem

We employ the Föppl membrane theory (i.e. the membrane limit of the Föppl–von Kármán equations) to describe the deformation of the elastic membrane [34,51]. Specifically, we adopt the formulation in terms of the Airy stress function ϕ and the transverse deflection w [52]. The out-of-plane equilibrium equation is then expressed as

$$\frac{1}{r}\frac{\mathrm{d}\phi}{\mathrm{d}r}\frac{\mathrm{d}w}{\mathrm{d}r} + \frac{\phi}{r}\frac{\mathrm{d}^2 w}{\mathrm{d}r^2} + q(r) = 0, \tag{3.1}$$

where $q(r)$ denotes the external transverse load acting on the membrane. The principal in-plane stress resultants are related to the Airy stress function through

$$N_{rr} = \frac{\phi}{r} \quad \text{and} \quad N_{\theta\theta} = \frac{\mathrm{d}\phi}{\mathrm{d}r}, \tag{3.2}$$

so that the in-plane equilibrium condition is automatically satisfied. To close the system, a geometric compatibility condition is required:

$$r\frac{\mathrm{d}}{\mathrm{d}r}\left[\frac{1}{r}\frac{\mathrm{d}}{\mathrm{d}r}(r\phi)\right] + \frac{1}{2}Et(w')^2 = 0, \tag{3.3}$$

where the prime denotes differentiation with respect to r.

As shown in figure 2b, the adhesive contact between the rigid sphere and the clamped membrane can be viewed, from a macroscopic perspective, as a mixed boundary value problem. The external load $q(r)$ enforces the membrane to conform to the spherical profile

$$w = \delta + R_s - \sqrt{R_s^2 - r^2} \approx \delta + \frac{r^2}{2R_s}, \tag{3.4}$$

for $r < a$, while $q(r) = p$ holds in the non-contact region ($r > a$). To facilitate computation, we first solve the inner region analytically by substituting equation (3.4) into equation (3.3), subject to the axisymmetric boundary conditions $w'(0) = 0$ and $N_{rr}(0) = N_{\theta\theta}(0)$. This yields the following continuity condition regarding the in-plane displacement at the contact line $r = a$:

$$\frac{\phi(a)}{a} - \phi'(a) = \frac{Eta^2}{8R_s^2}. \tag{3.5}$$

The problem is thus reduced to a single domain ($a < r < R_f$), although the contact radius a remains unknown and to be determined; consequently a total of five boundary conditions are required.

In addition to equation (3.5), the continuity of membrane deflection at the contact line requires

$$w(a) = \delta + \frac{a^2}{2R_s}. \tag{3.6}$$

At the clamped edge, both the deflection and the in-plane displacement are constrained by the applied pretension T_{pre}. Accordingly, the boundary conditions are

$$w(R_f) = 0 \quad \text{and} \quad \phi'(R_f) - \nu\frac{\phi(R_f)}{R_f} = (1-\nu)T_{\mathrm{pre}}. \tag{3.7}$$

The final missing condition is associated with determining the position of the contact line a, which follows from minimizing the total system energy according to equation (2.2). Alternatively, this condition has been shown to be equivalent to the discontinuity in the membrane slope across the contact line [51]. Specifically, in the absence of adhesion, the deflection slope remains continuous at $r = a$. The presence of adhesion, however, introduces a finite contact angle θ (figure 2b), which satisfies a Young's equation [44,53,54]:

$$N_{rr}^{-}(a) = N_{rr}^{+}(a)\cos\theta + \gamma, \tag{3.8}$$

where γ is the adhesion energy per unit area, and $N_{rr}^{-}(a)$ and $N_{rr}^{+}(a)$ denote the radial membrane tensions immediately inside and outside the contact line, respectively. Since the membrane tension is continuous across the contact line and the rotation is moderate, equation (3.8) can yield an approximate slope jump condition:

$$w'(a^-) - w'(a^+) \approx \sqrt{\frac{2\gamma a}{\phi(a)}}. \tag{3.9}$$

We shall solve equations (3.1) and (3.3) subject to the boundary conditions equations (3.5)–(3.9) numerically. To evaluate the corresponding external force, we consider the static equilibrium of the membrane by making an annular cut at any position in the non-contact region ($r > a$). The total pulling force is then given by

$$F = -2\pi a N_{rr}(a) w'(a^+) - \pi a^2 p = -2\pi\phi(a) w'(a^+) - \pi a^2 p, \tag{3.10}$$

where the cut is taken right outside the contact line ($r = a^+$).

(b) Non-dimensionalization

While it is natural to use the in-plane stiffness of the membrane, Et, for non-dimensionalization, the appropriate geometric length scales for rescaling are not immediately obvious. To address this, we introduce a macroscopic vertical length scale, δ_{macro} (to be specified shortly), and define the corresponding vertical and horizontal length scales as

$$\delta_* := \delta_{\mathrm{macro}} \quad \text{and} \quad a_* := \sqrt{\delta_{\mathrm{macro}} R_s}, \tag{3.11}$$

which follow the geometry of the sphere. Based on these, the governing variables are non-dimensionalized as

$$\bar{W} = \frac{w}{\delta_*}, \quad \bar{\Phi} = \frac{\phi}{Eta_*}, \quad \bar{R} = \frac{r}{a_*}, \quad \bar{\Delta} = \frac{\delta}{\delta_*}, \quad A = \frac{a}{a_*} \quad \text{and} \quad \mathcal{F} = \frac{F}{\pi\gamma R_s}, \tag{3.12}$$

and the problem is controlled by five non-dimensional parameters:

$$\bar{R}_f = \frac{R_f}{a_*}, \quad \bar{R}_s = \frac{R_s}{a_*}, \quad P = \frac{pR_s}{Et}, \quad \Gamma = \frac{\gamma}{Et} \quad \text{and} \quad \mathcal{T}_{\mathrm{pre}} = \frac{T_{\mathrm{pre}}}{Et}, \tag{3.13}$$

which describe, respectively, the membrane size, sphere radius, applied pressure, adhesion strength and pretension.

As such, the non-dimensional forms of the governing equations (3.1) and (3.3) are

$$\frac{1}{\bar{R}}\frac{\mathrm{d}\bar{\Phi}}{\mathrm{d}\bar{R}}\frac{\mathrm{d}\bar{W}}{\mathrm{d}\bar{R}}+\frac{\bar{\Phi}}{\bar{R}}\frac{\mathrm{d}^2\bar{W}}{\mathrm{d}\bar{R}^2}+P=0 \tag{3.14}$$

and

$$\frac{\mathrm{d}\bar{\Phi}}{\mathrm{d}\bar{R}}-\frac{\bar{\Phi}}{\bar{R}}+\bar{R}\frac{\mathrm{d}^2\bar{\Phi}}{\mathrm{d}\bar{R}^2}+\frac{1}{2\bar{R}_s^2}\left(\frac{\mathrm{d}\bar{W}}{\mathrm{d}\bar{R}}\right)^2=0. \tag{3.15}$$

Corresponding to equations (3.5)–(3.7), the associated boundary conditions can be expressed as

$$\bar{W}(A)=\bar{\Delta}+\frac{1}{2}A^2,\quad \bar{W}'(A^+)=A-\bar{R}_s\sqrt{\frac{2\Gamma A}{\bar{\Phi}(A)}}\quad\text{and}\quad \frac{\bar{\Phi}(A)}{A}-\bar{\Phi}'(A)=\frac{A^2}{8\bar{R}_s^2} \tag{3.16}$$

at the contact line and

$$\bar{W}(\bar{R}_f)=0\quad\text{and}\quad \bar{R}_f\bar{\Phi}'(\bar{R}_f)-\nu\bar{\Phi}(\bar{R}_f)=(1-\nu)\bar{R}_f\mathcal{T}_{\mathrm{pre}} \tag{3.17}$$

at the clamped outer edge. Finally, the dimensionless pulling force can be obtained from equation (3.10) as

$$\mathcal{F}=-\frac{2\bar{\Phi}(A)\bar{W}'(A^+)}{\Gamma\bar{R}_s^2}-\frac{PA^2}{\Gamma\bar{R}_s^2}. \tag{3.18}$$

(c) The macroscopic vertical length scale

Now we may specify a δ_{macro} to eliminate one of the five controlling parameters in equation (3.13)—for example, setting $\delta_{\mathrm{macro}}=R_s$ so that $\bar{R}_s=1$. However, rather than adopting a purely geometrical scaling, we prefer to define δ_* based on some physical considerations. This would enable a more meaningful comparison between the present macroscopic model and the microscopic model to be discussed in the next section.

The characteristic vertical length scale δ_* can be estimated by considering the spontaneous deflection of the membrane in adhesive contact with the sphere, where 'spontaneous' indicates that no external pulling force is applied. Adhesion is sufficient to induce a deflection δ_{macro} over a lateral scale $a_*\sim\sqrt{\delta_{\mathrm{macro}}R_s}$. The associated strain scales as $(\delta_*/a_*)^2$, and the corresponding elastic energy can be estimated as

$$U_{\mathrm{elastic}}\sim T_{\mathrm{total}}\frac{\delta_*^2}{a_*^2}\times a_*^2, \tag{3.19}$$

where T_{total} is the typical membrane tension in the contact region. This tension has three contributions: (i) the initial pretension T_{pre}, (ii) tension induced by pressurization,

$$T_p\sim(Etp^2R_f^2)^{1/3}, \tag{3.20}$$

and (iii) additional tension generated by the spontaneous deflection itself, scaling as $Et(\delta_*/a_*)^2$. A simple estimate of the total tension is therefore

$$T_{\mathrm{total}}\sim T_{\mathrm{pre}}+T_p+Et\left(\frac{\delta_*}{a_*}\right)^2. \tag{3.21}$$

This elastic energy must balance the adhesion energy, which scales as

$$U_{\mathrm{adhesion}}\sim\gamma a_*^2. \tag{3.22}$$

Equating U_{elastic} and U_{adhesion} yields a quadratic equation in terms of δ_*, and an explicit expression for the characteristic vertical deflection is ultimately obtained as

$$\delta_{\mathrm{macro}}=\frac{\sqrt{[(Etp^2R_f^2)^{1/3}+T_{\mathrm{pre}}]^2+4Et\gamma}-(Etp^2R_f^2)^{1/3}-T_{\mathrm{pre}}}{2Et/R_s}. \tag{3.23}$$

Of course, this definition of δ_{macro} can also be used to eliminate one of the controlling parameters in equation (3.13), albeit in a slightly more involved manner. By substituting the non-dimensional parameters from equation (3.13) into equation (3.23), we obtain

$$2\bar{R}_s^{-2} = \sqrt{\left(\frac{P^{2/3}}{\alpha^{2/3}} + \mathcal{T}_{\text{pre}}\right)^2 + 4\varGamma} - \frac{P^{2/3}}{\alpha^{2/3}} - \mathcal{T}_{\text{pre}}, \tag{3.24}$$

where

$$\alpha = \frac{\bar{R}_s}{\bar{R}_f} = \frac{R_s}{R_f} \tag{3.25}$$

represents the relative size of the sphere with respect to the membrane. Consequently, for a given α, the non-dimensional sphere radius $\bar{R}_s$ can be determined from equation (3.24), and the non-dimensional membrane radius $\bar{R}_f$ follows directly from equation (3.25).

It is now clear that the macroscopic model, as specified by equations (3.14)–(3.18), is exclusively governed by four dimensionless quantities: the adhesion energy $\varGamma$, the pretension $\mathcal{T}_{\text{pre}}$, the pressure P and the geometric parameter α. We solve this problem, defined over the domain $A < \bar{R} < \bar{R}_f$, numerically using the boundary value problem solver `bvp5c` in MATLAB. For a prescribed pulling displacement $\bar{\varDelta}$, the contact radius A would, in principle, be treated as unknown to satisfy all boundary conditions simultaneously. In practice, however, we found it more convenient to prescribe A and then solve for the corresponding pulling displacement from equation (3.16) and the required pulling force from equation (3.18) to achieve the desired contact radius.

In figure 3, we present the pulling force–displacement and pulling force–contact radius curves for various combinations of $\varGamma$, $\mathcal{T}_{\text{pre}}$, P and α. Consistent with previous findings [44], the maximum pulling force during detachment is given by

$$\mathcal{F}_c = 1, \tag{3.26}$$

that is, $F_c = \pi\gamma R_s$ in dimensional form, independent of the membrane size, sphere radius, adhesion strength or applied pressure. Here, we apply a sufficiently small pressure such that the curvature of the pressurized membrane remains much smaller than that of the sphere; otherwise, the pressurized geometry would influence the pull-off force [53]. Dashed curves in figure 3 denote the post-pull-off branches of the force–displacement and force–contact radius curves, which are inaccessible in force-controlled experiments owing to the jump-out-of-contact instability.

A notable feature in figure 3 is that, after rescaling the pulling displacement by δ_* and the contact radius by a_* as defined in equation (3.11), the corresponding $\bar{\varDelta}_c$ and A_c at the pull-off point are both approximately of order $O(1)$. For instance, this is evident in figure 3a,b, where the adhesion parameter $\varGamma$ varies over four orders of magnitude. These results justify the appropriateness of using the characteristic vertical length scale δ_{macro} defined in equation (3.23) for describing the macroscopic adhesion model. We now proceed to the microscopic adhesion model and its corresponding characteristic vertical length scale.

4. The microscopic adhesion model

(a) Governing equations

From a microscopic perspective, the sphere interacts with the membrane through intermolecular forces acting across the entire interfacial domain (see figure 2c). When the interfacial traction follows an LJ type law, as given in equation (2.3), the geometric compatibility equation (3.3) remains identical to that of the macroscopic model, while the vertical force balance in equation (3.1) is modified to

$$\frac{1}{r}\frac{\mathrm{d}\phi}{\mathrm{d}r}\frac{\mathrm{d}w}{\mathrm{d}r} + \frac{\phi}{r}\frac{\mathrm{d}^2 w}{\mathrm{d}r^2} + p + \frac{8\gamma}{3z_0}\left[\left(\frac{z_0}{g}\right)^3 - \left(\frac{z_0}{g}\right)^9\right] = 0, \tag{4.1}$$

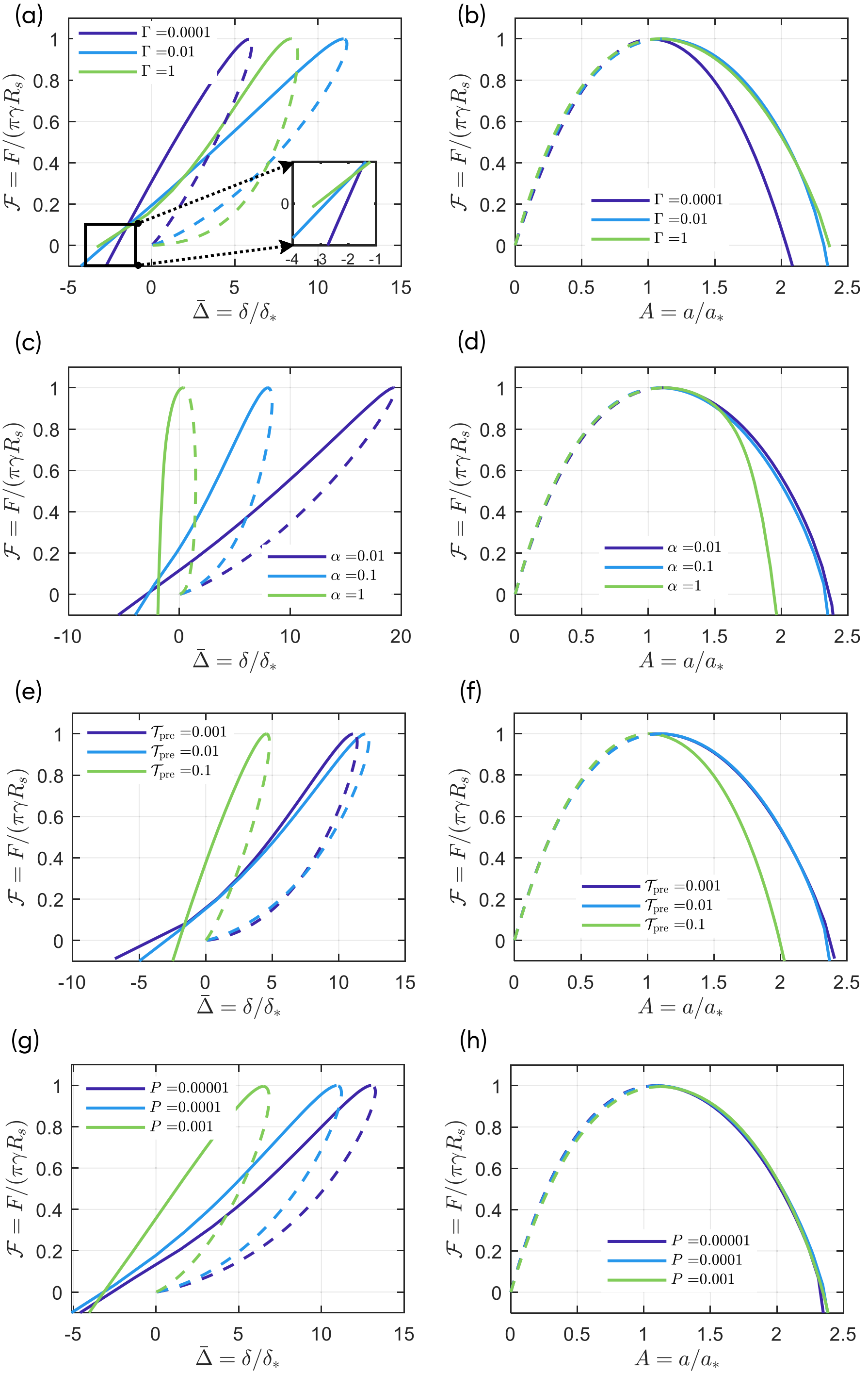

Figure 3. The macroscopic (JKR-type) adhesion model. (a,b) Rescaled pulling force–displacement and pulling force–contact radius curves computed for various adhesion energies Γ with $\alpha = 0.05$, $\mathcal{T}_{\rm pre} = 0.01$ and $P = 5 \times 10^{-5}$. The inset provides a magnified view near the zero external force point. (c,d) Rescaled pulling force–displacement and pulling force–contact radius curves computed for various sphere-to-membrane size ratios α with $\Gamma = 0.05$, $\mathcal{T}_{\rm pre} = 0.01$ and $P = 5 \times 10^{-5}$. (e,f) Rescaled pulling force–displacement and pulling force–contact radius curves computed for various pretensions $\mathcal{T}_{\rm pre}$ with $\Gamma = 0.05$, $\alpha = 0.05$ and $P = 5 \times 10^{-5}$. (g,h) Rescaled pulling force–displacement and pulling force–contact radius curves computed for various pressure levels P with $\Gamma = 0.05$, $\alpha = 0.05$ and $\mathcal{T}_{\rm pre} = 0.01$. Note that the definition of the controlling parameters can be found in equations (3.13) and (3.25).

for $0 \le r \le R_f$, where z_0 is the equilibrium separation between the two surfaces, and the local gap g is given by

$$g(r) = \delta + \frac{r^2}{2R_s} - w(r). \tag{4.2}$$

Here, the Derjaguin approximation has been employed [55]. The boundary conditions at the outer clamped edge in equation (3.7) remain unchanged, whereas at the origin, we impose symmetry and zero in-plane displacement, i.e.

$$w'(0) = 0 \quad \text{and} \quad \lim_{r\to 0}[r\phi'(r) - \nu\phi(r)] = 0. \tag{4.3}$$

The pulling force applied to the sphere is balanced by the net van der Waals traction acting over the entire interaction region, expressed as

$$F = \int_0^{R_f} \frac{8\gamma}{3z_0}\left[\left(\frac{z_0}{g}\right)^3 - \left(\frac{z_0}{g}\right)^9\right] 2\pi r\,\mathrm{d}r. \tag{4.4}$$

Different from the macroscopic model discussed in the preceding section, the microscopic model naturally provides a characteristic vertical length scale through the equilibrium separation of the interface, z_0. Accordingly, we define

$$\delta_* := \delta_{\text{micro}} = z_0 \quad \text{and} \quad a_* := \sqrt{z_0 R_s}, \tag{4.5}$$

and perform non-dimensionalization in a form analogous to equation (3.12), yielding

$$W = \frac{w}{z_0}, \quad \Phi = \frac{\phi}{Et\sqrt{z_0 R_s}}, \quad R = \frac{r}{\sqrt{z_0 R_s}}, \quad \Delta = \frac{\delta}{z_0} \quad \text{and} \quad G = \frac{g}{z_0}. \tag{4.6}$$

The associated dimensionless control parameters are then given by

$$\mathcal{R}_f = \frac{R_f}{\sqrt{z_0 R_s}}, \quad \mathcal{R}_s = \frac{R_s}{\sqrt{z_0 R_s}}, \quad P = \frac{pR_s}{Et}, \quad \Gamma = \frac{\gamma}{Et} \quad \text{and} \quad \mathcal{T}_{\text{pre}} = \frac{T_{\text{pre}}}{Et}. \tag{4.7}$$

Note that the definitions of the dimensionless pressure P, adhesion Γ and pretension $\mathcal{T}_{\text{pre}}$ remain identical to those used in the macroscopic formulation in equation (3.13).

We then present the dimensionless forms of equations (4.1) and (3.3):

$$\frac{1}{R}\frac{\mathrm{d}\Phi}{\mathrm{d}R}\frac{\mathrm{d}W}{\mathrm{d}R^2} + \frac{\Phi}{R}\frac{\mathrm{d}^2W}{\mathrm{d}R} + P + \frac{8}{3}\Gamma\mathcal{R}_s^2\left(\frac{1}{G^3} - \frac{1}{G^9}\right) = 0 \tag{4.8}$$

and

$$\frac{\mathrm{d}\Phi}{\mathrm{d}R} - \frac{\Phi}{R} + R\frac{\mathrm{d}^2\Phi}{\mathrm{d}R^2} + \frac{1}{2\mathcal{R}_s^2}\left(\frac{\mathrm{d}W}{\mathrm{d}R}\right)^2 = 0, \tag{4.9}$$

where the dimensionless interfacial gap G is expressed as

$$G(R) = \Delta + \frac{1}{2}R^2 - W(R). \tag{4.10}$$

The boundary conditions equations (4.3) and (3.7) become

$$W'(0) = 0 \quad \text{and} \quad \lim_{R\to 0}[R\Phi'(R) - \nu\Phi(R)] = 0 \tag{4.11}$$

at the origin and

$$W(\mathcal{R}_f) = 0 \quad \text{and} \quad \mathcal{R}_f\Phi'(\mathcal{R}_f) - \nu\Phi(\mathcal{R}_f) = (1-\nu)\mathcal{R}_f\mathcal{T}_{\text{pre}} \tag{4.12}$$

at the edge. The dimensionless pulling force is given by

$$\mathcal{F} = \frac{16}{3}\int_0^{\mathcal{R}_f}\left(\frac{1}{G^3} - \frac{1}{G^9}\right) R\,\mathrm{d}R, \tag{4.13}$$

which reaches a maximum value of 2 when the membrane is perfectly rigid ($W = 0$), consistent with the classical Bradley limit.

The coupled nonlinear equations (4.8)–(4.13) are solved numerically using a finite-difference scheme combined with the Newton–Raphson iteration method (see details in appendix A). Clearly, the entire microscopic system is governed by the five dimensionless quantities defined in equation (4.7), which contain one additional parameter compared with the macroscopic model owing to the introduction of the interfacial equilibrium length scale z_0. Since the controlling parameters P, Γ and $\mathcal{T}_{\mathrm{pre}}$ are identical to both models, the essential distinction lies in their geometric characterization: the microscopic model features two independent ratios, $\mathcal{R}_s$ and $\mathcal{R}_f$, whereas the macroscopic model is described by a single geometric parameter α. To make a fair comparison between the two frameworks, we need to set $\alpha = \mathcal{R}_s/\mathcal{R}_f$ while keeping P, Γ and $\mathcal{T}_{\mathrm{pre}}$ identical. However, this correspondence is not unique—infinitely many pairs of $(\mathcal{R}_s, \mathcal{R}_f)$ can yield the same α. Intriguing questions then arise: how do different microscopic combinations (leading to the same macroscopic geometry) influence the system's behaviour, and to what extent do their predictions deviate from those of the macroscopic model?

(b) Transition parameters

To address the questions posed above, it is essential to establish a bridge between the macroscopic and microscopic perspectives of adhesion illustrated in figure 2. Since each model possesses its own characteristic lengths defined in equations (3.11) and (4.5), respectively, a natural way to connect them is through the ratio of these lengths:

$$\lambda = \frac{\delta_{\mathrm{macro}}}{\delta_{\mathrm{micro}}} = \left[\sqrt{\left[\left(\frac{pR_f}{Et}\right)^{2/3} + \frac{T_{\mathrm{pre}}}{Et}\right]^2 + \frac{4\gamma}{Et}} - \left(\frac{pR_f}{Et}\right)^{2/3} - \frac{T_{\mathrm{pre}}}{Et}\right]\frac{R_s}{2z_0}. \tag{4.14}$$

Clearly, physical quantities involved in λ are physically transparent. We show shortly that reducing the membrane's apparent stiffness—through a decrease in pressure, pretension or intrinsic modulus—or increasing the sphere radius leads to a larger value of λ. Physically, the condition $\lambda \gg 1$ indicates that the spontaneous deflection of the membrane, δ_{macro}, induced by adhesion is much greater than the equilibrium separation δ_{micro} (i.e. z_0). In this regime, microscopic details at the scale of z_0 become negligible, and one may expect the formation of a well-defined 'contact zone', as illustrated in figure 2b. The overall adhesion behaviour, therefore, should approach that described by the macroscopic (JKR-type) adhesion model. Conversely, when the membrane becomes effectively rigid and the microscopic length dominates ($\lambda \ll 1$), the equilibrium separation z_0 far exceeds the spontaneous deflection δ_*, and the adhesion behaviour tends towards the Bradley rigid-body limit. In this sense, λ quantifies the relative flexibility of the membrane compared with the adhesive strength.

The classical Tabor parameter for elastic slabs is expressed as $\mu = R^{1/3}\gamma^{2/3}/(E_*^{2/3}z_0)$, where R and E_* are the equivalent radius and the elastic modulus, respectively. It can also be viewed as a comparison between macroscopic characteristic length $R^{1/3}\gamma^{2/3}/E_*^{2/3}$ and the microscopic length z_0 [9,15]. Therefore, λ defined here is conceptually analogous to the Tabor parameter μ for elastic slabs. We thus regard λ as a generalized Tabor parameter for elastic membranes. Note, however, that owing to the unique geometric characteristics of the membrane, parameter λ involves a greater number of physical quantities, making its specific expression considerably more complex than that of the Tabor parameter μ.

As discussed above, the membrane may appear rigid under indentation owing to three distinct factors: its intrinsic stiffness, the applied pretension and the external pressure. We may clarify their individual contributions to the generalized Tabor parameter by examining each effect separately. For example, in the absence of pretension and pressure, equation (3.23) simplifies to $\delta_{\mathrm{macro}} = R_s\sqrt{\gamma/Et}$. Comparing this to the microscopic equilibrium separation z_0 yields

$$\lambda_E = \sqrt{\frac{\gamma}{Et}}\frac{R_s}{z_0} = \sqrt{\Gamma}\mathcal{R}_s^2, \tag{4.15}$$

which quantifies the role of the intrinsic membrane stiffness. Similarly, the contribution of the pretension can be represented as

$$\lambda_T = \frac{\gamma R_s}{T_{\mathrm{pre}} z_0} = \frac{\varGamma \mathcal{R}_s^2}{\mathcal{T}_{\mathrm{pre}}}, \tag{4.16}$$

and that of the external pressure as

$$\lambda_p = \frac{\gamma R_s}{(Etp^2 R_f^2 z_0^3)^{1/3}} = \frac{\varGamma \mathcal{R}_s^{8/3}}{P^{2/3} \mathcal{R}_f^{2/3}}. \tag{4.17}$$

The generalized Tabor parameter can then be rewritten as a combined measure:

$$\lambda = \frac{2}{\sqrt{((1/\lambda_p) + (1/\lambda_T))^2 + (2/\lambda_E)^2} + 1/\lambda_p + 1/\lambda_T}. \tag{4.18}$$

This highlights that the apparent rigidity of the membrane is dictated by the most dominant stiffening mechanism: whenever any of the subparameters is small, the overall λ becomes small, pushing the system towards the rigid (Bradley-like) limit. Interestingly, we find that the problem can be rescaled such that the number of independent controlling parameters is reduced from five, as defined in equation (4.7), to four (λ_E, λ_T, λ_p and $\mathcal{R}_f$); see appendix B.

(c) Microscopic-to-macroscopic transition

In this section, we systematically vary the magnitude of each subparameter while keeping the other two sufficiently large. This strategy enables us to isolate and quantify the distinct roles of the intrinsic stiffness, pretension and external pressure in governing the adhesion behaviour of elastic membranes. The combined effects arising from mixed variations of these subparameters will be analysed in the subsequent section.

(i) Transition caused by intrinsic stiffness

We first investigate the influence of the intrinsic membrane stiffness, characterized by the parameter λ_E. To this end, the pretension and pressure are both set to zero ($\mathcal{T}_{\mathrm{pre}} = P = 0$), so that λ_T and λ_p approach infinity, yielding $\lambda = \lambda_E$. The corresponding pull-off force $\mathcal{F}_c$ as a function of λ_E is shown in figure 4a. Notably, although the calculations are performed for specific values of $\varGamma$ and $\mathcal{R}_s$, the results expressed in terms of λ_E are essentially independent of $\mathcal{R}_s$. Moreover, they exhibit negligible sensitivity to $\mathcal{R}_f$; for example, the $\mathcal{F}_c$–λ_E curves obtained with $\mathcal{R}_f = 20$ and 500 nearly coincide in figure 4a.

In figure 4a, a clear microscopic-to-macroscopic transition is observed. As λ_E increases from 10^{-3} to 10^2, the pull-off force $\mathcal{F}_c$ decreases from $2\pi\gamma R_s$ (the Bradley limit) to $\pi\gamma R_s$ (the JKR-type limit). The corresponding configurations of the membrane at the pull-off point for these two limits are illustrated in the insets of figure 4a. According to equation (4.15), this transition can be experimentally realized by decreasing the membrane stiffness or, equivalently, by increasing either the sphere radius or the adhesion energy.

We further examine the pulling force–displacement responses for various values of λ_E, as shown in figure 4b,c. As λ_E decreases, the force–displacement curve gradually approaches the Bradley limit, in which the pull-off process is smooth. When λ_E exceeds a critical value, however, jump-in and jump-out instabilities emerge (see the dashed curves in figure 4b), similar to the behaviour observed for elastic slabs [11]. With a further increase in λ_E, the numerical results obtained from the microscopic adhesion model converge towards those from the macroscopic (JKR-type) adhesion model, as indicated by the dash-dotted curves in figure 4c. Note that in the absence of pretension and pressure, this transition is governed solely by λ_E, as defined in equation (4.15), almost independent of the specific geometrical values of $\mathcal{R}_s$ and $\mathcal{R}_f$.

To further elucidate this transition, we examine the detailed membrane deflection for λ_E ranging from 1 to 100, as shown in figure 5. To avoid scale distortion of the rigid sphere caused by

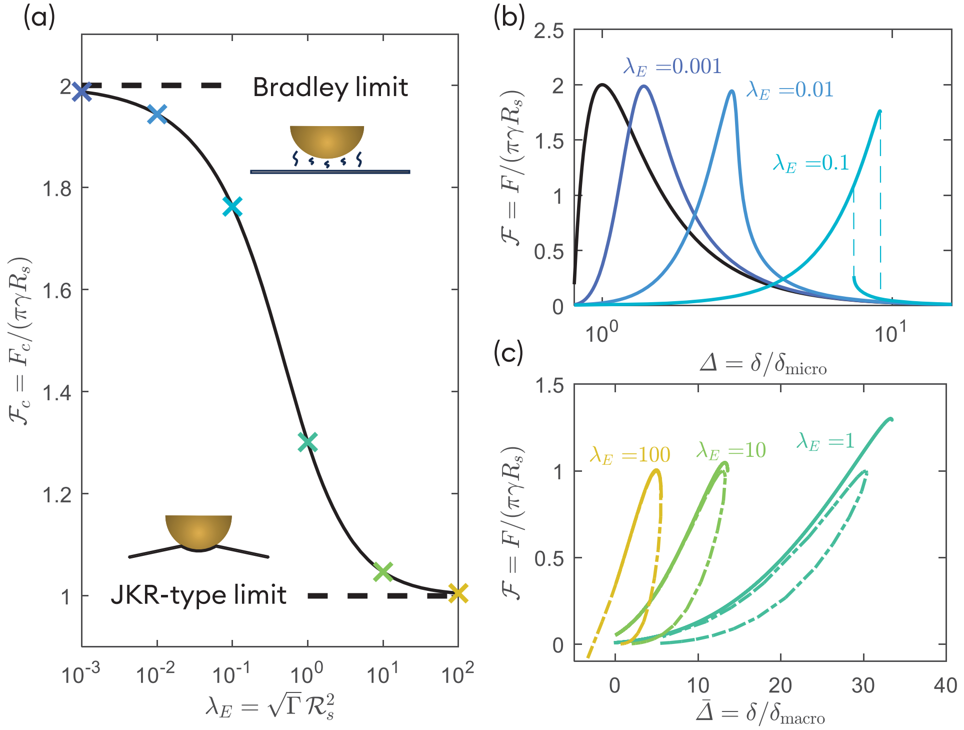

Figure 4. Microscopic-to-macroscopic transition induced by the intrinsic membrane stiffness. (a) Numerical results of the pull-off force for varying λ_E (obtained by adjusting Γ with $\mathcal{R}_s = 20$, $\mathcal{R}_f = 100$, $P = 0$ and $\mathcal{T}_{\mathrm{pre}} = 0$). The insets illustrate the membrane configurations at the pull-off point for the microscopic (Bradley) and macroscopic (JKR-type) limits. (b,c) Pulling force–displacement curves computed for different values of λ_E, with curve colours corresponding to the cross-shaped markers in (a). The black curve in (b) represents the Bradley limit, while the dash-dotted curves in (c) show the corresponding results from the macroscopic adhesion model using the same set of controlling parameters and $\alpha = \mathcal{R}_s/\mathcal{R}_f$.

different non-dimensional treatments in the horizontal and vertical directions, all quantities are plotted in their dimensional units (using $R_f = 2000\,\mathrm{nm}$, $R_s = 400\,\mathrm{nm}$, $Et = 340\,\mathrm{N/m}$, $z_0 = 1\,\mathrm{nm}$ and $\gamma = 2.125 \times 10^{-3}$, 2.125×10^{-1} and 2.125×10^{1} nm, respectively). As λ_E increases, corresponding to larger adhesion energy γ, the membrane exhibits progressively larger deflections, such that the fine details of the interfacial gap near the centre become negligible compared with the overall deformation (figure 5a). The resulting profile naturally divides into two regions: an inner region that nearly conforms to the spherical surface and an outer region that rapidly detaches from it.

This observation motivates the introduction of a contact line in the microscopic adhesion model to delineate the two regions. Specifically, we define the contact line as the position where the van der Waals traction attains its maximum value, which conceptually corresponds to the stress singularity at the edge of the JKR contact [1]. At this location, the gap satisfies $g/z_0 = 3^{1/6} \approx 1.2$ (indicated by the dashed line in figure 5b). Within the contact zone, the surface gap remains nearly uniform and of the order of the equilibrium distance z_0, while the interfacial LJ potential energy is of the order of the adhesion strength γ. In contrast, in the non-contact zone, the gap increases rapidly, leading to a sharp decay of the interfacial potential (figure 5b,c). When the total interfacial potential energy over the entire membrane is compared with the nominal JKR-type adhesion energy $\pi\gamma a^2$, their ratio approaches unity as λ_E increases (figure 5d). Consequently, the adhesion behaviour asymptotically approaches the JKR-type limit, in which the interfacial separation within the contact region can be neglected and the adhesion strength is effectively uniform across the contact area, while the exterior region becomes essentially non-interacting. Based on the above analysis, we may obtain an additional qualitative physical interpretation of

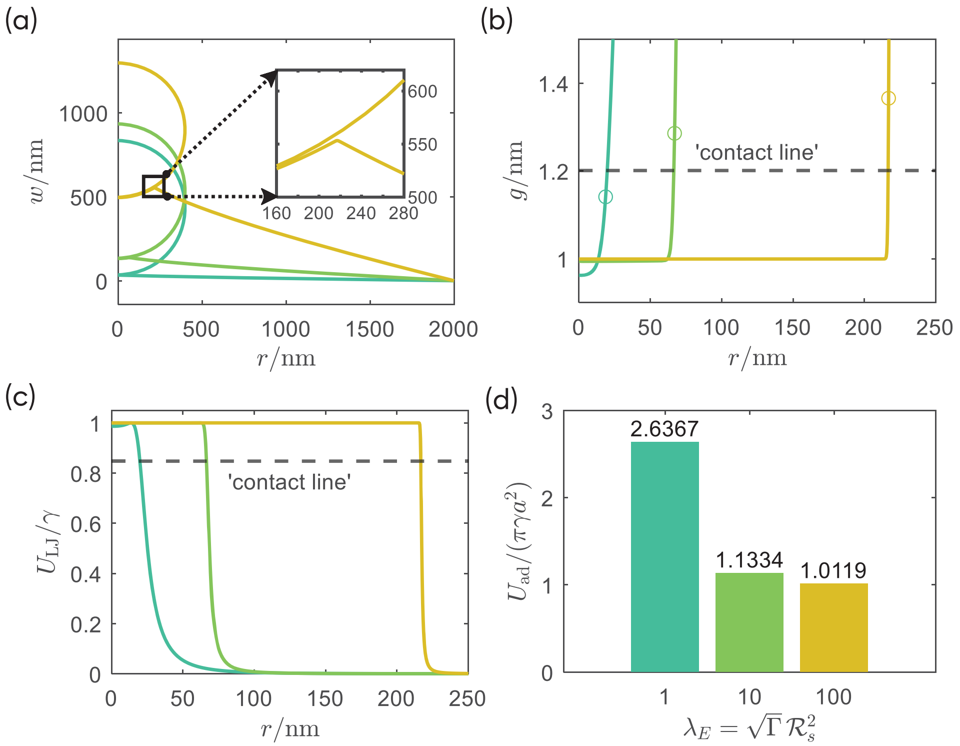

Figure 5. Detailed analysis of the membrane deformation for $\lambda_E = 1$, 10 and 100 (curve colours correspond to those in figure 4c). (a) Membrane profiles at the maximum pull-off force. The inset shows an enlarged view of the region near the contact line for $\lambda_E = 100$. (b) Interfacial gap distribution near the membrane centre. The dashed line indicates the gap where the van der Waals traction reaches its maximum value ($d = 3^{1/6}z_0$), and the circular markers denote the radii at which the membrane attains its highest point. (c) Distribution of the local interfacial LJ potential energy ($U_{\mathrm{LJ}}(r) = \int_g^\infty \sigma_{\mathrm{adh}}\mathrm{d}z$) relative to adhesion γ. The dashed line marks the relative potential energy evaluated at the contact line. (d) Ratio of the total interfacial potential energy over the entire membrane ($U_{\mathrm{ad}} = \int_0^{R_f} U_{\mathrm{LJ}}(r)2\pi r\mathrm{d}r$) to the JKR-type adhesion energy within the contact region, plotted as a function of λ_E.

λ_E: it characterizes the relative size of the 'process zone' of the adhesive energy U_{LJ} outside the contact region. In essence, it represents the ratio of the macroscopic to microscopic horizontal characteristic length scales.

(ii) Transition caused by pretension

We now examine the effect of pretension on the adhesion behaviour. When λ_T is much smaller than the other two subparameters, the overall Tabor parameter can be approximated as $\lambda \approx \lambda_T$. We then keep the geometric parameters unchanged ($R_f = 2000\,\mathrm{nm}$ and $R_s = 400\,\mathrm{nm}$), set the external pressure to zero ($P = 0$) and fix the intrinsic stiffness at a sufficiently small value ($Et = 0.016\,\mathrm{N\,m^{-1}}$ with $\gamma = 0.1\,\mathrm{N\,m^{-1}}$ and $z_0 = 1\,\mathrm{nm}$) such that $\lambda_E = 1000$ and $\lambda_p = \infty$. We then vary the pretension $\mathcal{T}_{\mathrm{pre}}$ while keeping all other parameters constant, thereby eliminating the influence of intrinsic stiffness and external pressure. The corresponding numerical results for $\mathcal{R}_f = 100$ are presented in figure 6.

The evolution of the adhesion behaviour dominated by λ_T closely mirrors that governed by λ_E. As λ_T increases (equivalently, as the pretension $\mathcal{T}_{\mathrm{pre}}$ decreases), the pull-off force decreases from $2\pi\gamma R_s$ (the Bradley limit) to $\pi\gamma R_s$ (the JKR-type limit). This trend demonstrates that the membrane pretension $\mathcal{T}_{\mathrm{pre}}$ effectively tunes the adhesion response, consistent with previous analyses and experimental measurements [45,47]. Moreover, the dimensionless $\mathcal{F}_c$–λ_T relation is

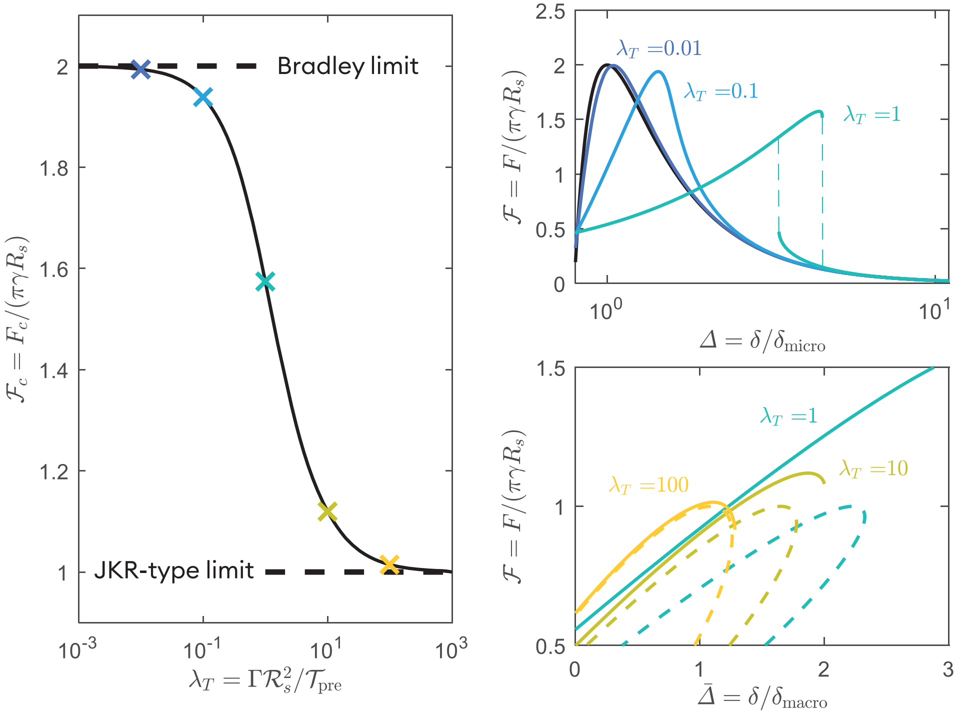

Figure 6. Microscopic-to-macroscopic transition induced by the pretension. (a) Numerical results of the pull-off force for varying λ_T at $\lambda_E = 1000$ (obtained by adjusting $\mathcal{T}_{\rm pre}$ with $\mathcal{R}_s = 20$, $\mathcal{R}_f = 100$, $P = 0$ and $\Gamma = 6.25$). (b) Pulling force–displacement curves and (c) the enlarged view computed for different values of λ_T, with curve colours corresponding to the cross-shaped markers in (a). The black curve in (b) represents the Bradley limit, while the dash-dotted curves in (c) show the corresponding results from the macroscopic adhesion model using the same set of controlling parameters and $\alpha = \mathcal{R}_s/\mathcal{R}_f$.

nearly insensitive to the membrane radius $\mathcal{R}_f$, as the results for different $\mathcal{R}_f$ values with $\mathcal{R}_f = 20$ and $\mathcal{R}_f = 500$ almost coincide in figure 6a.

(iii) Transition caused by transverse pressure

The effect of transverse pressure, represented by the subparameter λ_p, exhibits a behaviour distinct from that governed by λ_E or λ_T. In principle, a sufficiently large λ_E would suppress the influence of the membrane stiffness Et and isolate the contribution of λ_p. However, excessively large λ_E values lead to numerical instability. To maintain computational robustness while preserving physical relevance, we therefore set $\lambda_E = 1$ and explore the entire range $\lambda_p \in [10^{-3}, 10^3]$. For clarity, this range is divided into two regimes (figure 7): the λ_E-dominated domain (blue region; $\lambda_E \ll \lambda_p$) and the λ_p-dominated domain (yellow region; $\lambda_p \ll \lambda_E$).

In the λ_E-dominated domain, increasing λ_p has little influence on the pull-off force, which remains nearly constant and converges to the value indicated by the green cross-shaped marker in figure 7. This point corresponds to the same pull-off force as that for $\lambda_E = 1$ in figure 4a (same colour), confirming that in this regime, λ is very close to λ_E and $\lambda_E = 1$ is not sufficiently large to drive the transition towards the JKR-type limit. Again, the results are nearly insensitive to the membrane radius $\mathcal{R}_f$, consistent with the trends observed in the previous subsections.

In the λ_p-dominated domain, however, a qualitatively different behaviour emerges. As λ_p decreases (or equivalently, as the external pressure P increases), the pull-off force no longer rises towards the Bradley limit but instead begins to decrease. This reduction is strongly dependent on the membrane radius $\mathcal{R}_f$: a smaller $\mathcal{R}_f$ yields a lower maximum pull-off force, and the critical λ_p at which the force begins to drop shifts to higher values. This phenomenon can be attributed

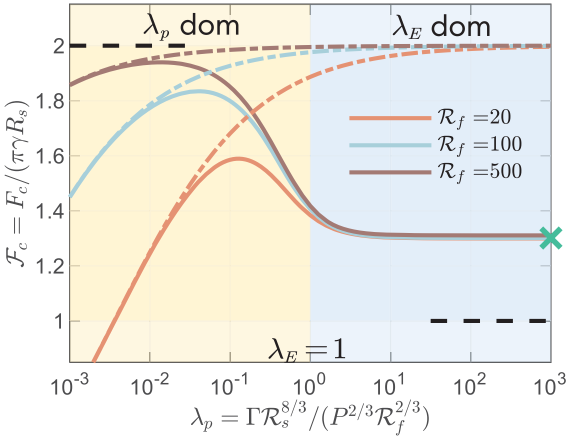

Figure 7. Influence of the pressure subparameter λ_p at $\lambda_E = 1$ and $\lambda_T = \infty$ for $\mathcal{R}_f \in \{20, 100, 500\}$ and $\mathcal{R}_s = 20$. The solid curves represent the numerical results, and the dash-dotted curves are the solutions of the pressurized Bradley model. The plot is partitioned at $\lambda_p = 1$ into a λ_E-dominated domain (blue region; $\lambda_p \gg 1$) and a λ_p-dominated domain (yellow region; $\lambda_p \ll 1$). The green cross-shaped marker matches the marker of the same colour in figure 4a.

to the pressurization-induced deformation of the membrane, or equivalently, to the increase in the local curvature near the centre, which enlarges the interfacial spacing and weakens the van der Waals attraction. The ratio of the membrane's central curvature to that of the sphere scales as $\beta \sim \delta_p R_s/R_f^2$, which can be rewritten as $\beta \sim \lambda_E/(\lambda_p^{1/2}\mathcal{R}_f)$. At constant λ_E, smaller λ_p or $\mathcal{R}_f$ thus produce a larger β, indicating a stronger curvature effect and a corresponding reduction in adhesion strength.

To verify this interpretation, we introduce a pressurized Bradley model, consisting of a rigid sphere in contact with a rigidly bulged membrane. Unlike the conventional Bradley model, the membrane in this case exhibits an initial curvature induced by the applied pressure, and the subsequent effects of van der Waals traction on the membrane's shape are neglected, which procedurally shares similarities with the DMT model. The corresponding computational approach involves first determining the membrane's shape under pure pressure, and then using this as the foundation to calculate the net force arising from the van der Waals interaction. The corresponding numerical solutions of the pressurized Bradley model for different $\mathcal{R}_f$ are plotted as dash-dotted curves in figure 7. This model reproduces the observed trends: as λ_p decreases, the numerical results progressively converge towards the pressurized Bradley limit, where the pull-off force is dominated by the geometric curvature rather than by elastic deformation. Fortunately, in most practical situations [31,32], spheres with relatively large curvature radii are employed, so the effect of the membrane's pressurized curvature can be safely neglected. In other words, for weakly pressurized systems, the role of λ_p is qualitatively similar to that of λ_E and λ_T in the microscopic-to-macroscopic transition, although λ_p is generally insufficient to induce a complete transition.

5. The generalized Tabor parameter

After the separate analyses described above, we now combine all three subparameters to demonstrate that λ serves as the unified governing parameter of the system. To this end, we consider a series of dimensionless pretensions $\mathcal{T}_{\mathrm{pre}}$, pressures P and adhesion energies Γ, together with varying geometrical parameters $\mathcal{R}_f$ and $\mathcal{R}_s$ to systematically modulate λ. Note that the dimensionless pressure is constrained by $P \lesssim \beta^3\mathcal{R}_f^2/\mathcal{R}_s^2$ to minimize the influence of the curvature of the bulged membrane, where the curvature ratio is fixed at $\beta = 1\%$. The resulting numerical solutions are presented in figure 8. It can be seen that under various parameter settings, including

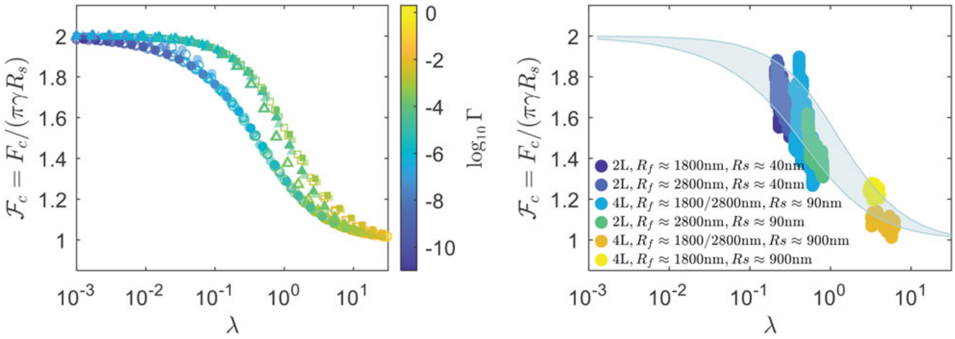

Figure 8. (a) Variation of the pull-off force for a series of parameter combinations: pretension $\mathcal{T}_{\text{pre}} \in \{0, 0.01, 0.1\}$ (represented by circular, upper-triangular and square markers, respectively); pressure $P \in \{0, 10^{-6}\}$ (denoted by opaque and semi-transparent markers); adhesion energy Γ (indicated by colour according to the accompanying colour bar); and geometric parameters $\mathcal{R}_f \in \{20, 100\}$ (represented by small and large markers) and $\mathcal{R}_s \in \{10, 20\}$ (represented by unfilled and filled markers). (b) Envelope of the numerical results shown in (a) compared with experimental data reported by Yu *et al.* [31], where L, R_f and R_s represent the number of graphene layers, the radius of the substrate cavity and the radius of the indenter, respectively.

Γ, P, $\mathcal{R}_s$, $\mathcal{R}_f$ and $\mathcal{T}_{\text{pre}}$, the calculated results exhibit a smooth transition from the Bradley limit ($2\pi\gamma R_s$) to the JKR-type limit ($\pi\gamma R_s$) as λ increases. This confirms that λ effectively captures the combined effects of elasticity, pretension and pressure, and thus serves as the overall control parameter governing membrane adhesion.

The envelopes of the numerical data points in figure 8a are further compared with the experimental measurements reported by Yu *et al.* [31], as shown in figure 8b. In these experiments, the pull-off forces were measured for suspended graphene membranes with different layer numbers, two membrane radii and three indenter radii, subjected to various transverse pressures. The pull-off force was observed to increase with applied pressure for measurements using small indenter radii, but to remain nearly unchanged for larger indenter radii. This apparent contrast can be rationalized by expressing the experimental data as a function of the generalized Tabor parameter λ defined in equation (4.14), as shown in figure 8b. For large indenter radii (yellow and orange markers), λ lies in the macroscopic domain ($\lambda > 1$), where the transition towards the microscopic regime is limited even with increasing pressure. In contrast, for small indenter radii, λ ranges from 0.1 to 1, corresponding to the regime in which the macroscopic-to-microscopic transition is most pronounced. As a result, even a modest increase in pressure—and hence a small decrease in λ—can lead to a discernible increase in the pull-off force. Note that nearly all experimental data points fall within the envelop curves, indicating that our model demonstrates a certain degree of accuracy in predicting pull-off forces at $\lambda \sim O(1)$.

6. Conclusion

We have discussed a unified model to elucidate the adhesion mechanics between a rigid sphere and an elastic membrane. By systematically analysing the individual and combined effects of the intrinsic stiffness, pretension and transverse pressure, we have identified the underlying mechanisms that govern the transition between the microscopic (Bradley-type) and macroscopic (JKR-type) adhesion regimes. Central to this framework is the introduction of a generalized Tabor parameter λ, which incorporates three distinct subparameters—λ_E, λ_T and λ_p—representing, respectively, the contributions from the membrane elasticity, pretension and pressure-induced tension. It should be emphasized that this single dimensionless parameter is physically transparent and quantitatively bridges the two limiting regimes and predicts the continuous evolution of the pull-off force from $2\pi\gamma R_s$ to $\pi\gamma R_s$ as λ increases. The model further captured the experimentally observed 'stiffer-is-stickier' behaviour of pressurized graphene membranes [31], where the pull-off force increases with effective tension for measurements using relatively small indenter sizes. The comparison between theoretical predictions and experimental measurements revealed good agreement, validating the robustness and physical generality of the proposed framework.

While the present work focuses on the membrane limit, several important directions merit further investigation. (i) For ultrathin yet finite-thickness films, the interplay between bending rigidity and in-plane tension may significantly alter the local contact geometry and the effective transition parameter. Extending the current model to the Föppl–von Kármán plate regime would thus enable a continuous connection between plate adhesion and membrane adhesion [27,28,37]. (ii) Many practical systems exhibit viscoelastic or thermally activated behaviour, which influences both the approach and detachment processes. Incorporating rate-dependent surface traction laws and temperature-dependent adhesion energy would provide predictive insight into time-dependent or hysteretic adhesion phenomena [56–59]. (iii) Realistic membranes often adhere to rough or patterned substrates, resulting in complex contact morphologies. Extending the present axisymmetric formulation to account for in-plane heterogeneity or multiple contact zones would broaden the applicability of the framework to microstructured and biological interfaces [60,61].

Data accessibility. MATLAB code for the microscopic adhesion model will be available in https://github.com/Weijia-Zeng/2025_generalized_Tabor_parameter.

Declaration of AI use. Yes, we have used AI-assisted technologies in creating this article. During the preparation of this manuscript, the authors used ChatGPT to polish the language. After using this tool/service, the authors reviewed and edited the content as needed and assume full responsibility for the content of the publication.

Authors' contributions. W.Z.: data curation, formal analysis, investigation, methodology, writing—original draft; Z.D.: conceptualization, formal analysis, funding acquisition, investigation, supervision, writing—original draft, writing—review and editing; Y.W.: conceptualization, funding acquisition, project administration, supervision, writing—review and editing.

All authors gave final approval for publication and agreed to be held accountable for the work performed therein.

Conflict of interest declaration. We declare we have no competing interests.

Funding. This work was supported by the National Natural Science Foundation of China (grant nos. 12372103 and 12432003).

Appendix A. Numerical method

We employ the finite-difference method combined with the Newton–Raphson iteration method to solve the highly nonlinear, coupled equations (4.8)–(4.13). The computational domain $R \in [0, \mathcal{R}_f]$ is discretized into n uniform intervals, resulting in $n+1$ nodes labelled from 0 to n. The unknown quantities are represented as vectors $\boldsymbol{W} = (W_0, W_1, \ldots, W_n)$ and $\boldsymbol{\Phi} = (\Phi_0, \Phi_1, \ldots, \Phi_n)$. Consequently, the governing equations (4.8) and (4.9) are discretized using a central-difference scheme, yielding a system of algebraic equations $f_k(\boldsymbol{W}, \boldsymbol{\Phi})$ and $g_k(\boldsymbol{W}, \boldsymbol{\Phi})$ for indices $(k = 1, \ldots, n-1)$:

$$f_k = \frac{1}{R_k}\frac{\Phi_{k+1}-\Phi_{k-1}}{2\Delta R}\frac{W_{k+1}-W_{k-1}}{2\Delta R} + \frac{\Phi_k}{R_k}\frac{W_{k+1}-2W_k+W_{k-1}}{\Delta R^2} + P + \frac{8}{3}\Gamma\mathcal{R}_s^2\left(\frac{1}{(\Delta+(1/2)R_k^2-W_k)^3} - \frac{1}{(\Delta+(1/2)R_k^2-W_k)^9}\right) = 0 \tag{A 1}$$

and

$$g_k = \frac{\Phi_{k+1}-\Phi_{k-1}}{2\Delta R} - \frac{\Phi_k}{R_k} + R_k\frac{\Phi_{k+1}-2\Phi_k+\Phi_{k-1}}{\Delta R^2} + \frac{1}{2\mathcal{R}_s^2}\left(\frac{W_{k+1}-W_{k-1}}{2\Delta R}\right)^2 = 0, \tag{A 2}$$

where $\Delta R = \mathcal{R}_f/n$ specifies the uniform grid spacing, and R_k denotes the node position with $R_n = \mathcal{R}_f$. The boundary conditions at the domain edges, coupling boundary values with interior nodes via equations (4.11) and (4.12), are expressed as

$$\frac{-3W_0+4W_1-W_2}{2\Delta R}=0 \quad \text{and} \quad R_k\frac{\Phi_0-2\Phi_1+\Phi_2}{\Delta R^2}-\nu\Phi_1=0 \tag{A 3}$$

and

$$W_n=0 \quad \text{and} \quad \mathcal{R}_f\frac{\Phi_{n-2}-4\Phi_{n-1}+3\Phi_n}{2\Delta R}-\nu\Phi_n=(1-\nu)\mathcal{R}_f\mathcal{T}_{\text{pre}}. \tag{A 4}$$

To ensure second-order discrete accuracy, a specific backward-difference scheme is employed at the boundary. In addition, the boundary condition for Φ at the central point is transformed into a coupling condition at node 1. When the mesh density is sufficiently refined, this approximation effectively captures the limiting behaviour at the centre without introducing significant errors.

The iterative process is as follows:

$$\begin{bmatrix}\Delta \boldsymbol{W}\\ \Delta \boldsymbol{\Phi}\end{bmatrix}=\begin{bmatrix}\frac{\partial f}{\partial \boldsymbol{W}} & \frac{\partial f}{\partial \boldsymbol{\Phi}}\\ \frac{\partial g}{\partial \boldsymbol{W}} & \frac{\partial g}{\partial \boldsymbol{\Phi}}\end{bmatrix}^{-1}\begin{bmatrix} f\\ g\end{bmatrix}, \tag{A 5}$$

where the Jacobi matrix is obtained by differentiating the algebraic expressions f_k and g_k with respect to each variable. The iterative process is considered converged when the norm of the relative step size falls a relative tolerance ϵ (set to be 10^{-8}):

$$\left\{\sum_{k=1}^{n-1}\left[\left(\frac{\Delta W_k}{W_k}\right)^2+\left(\frac{\Delta\Phi_k}{\Phi_k}\right)^2\right]\right\}^{1/2}<\epsilon. \tag{A 6}$$

Based on the calculated transverse deflection $\boldsymbol{W}$, the external force acting on the sphere is obtained using equation (4.13):

$$\mathcal{F}=\frac{1}{2}\left[\sum_{k=0}^{n-1}\frac{16}{3}(R_k\xi_k+R_{k+1}\xi_{k+1})\right]\Delta R, \tag{A 7}$$

where $\xi_k=1/(\Delta+\frac{1}{2}R_k^2-W_k)^3-1/(\Delta+\frac{1}{2}R_k^2-W_k)^9$.

Appendix B. Rescaled microscopic model

Using the rescaling $\Psi=\Phi\mathcal{R}_s^2$, the nonlinear boundary value problem defined by equations (4.8)–(4.12) can be expressed in terms of the three subparameters λ_E, λ_T and λ_p as

$$\frac{\Psi}{R}\frac{\mathrm{d}^2W}{\mathrm{d}R^2}+\frac{1}{R}\frac{\mathrm{d}\Psi}{\mathrm{d}R}\frac{\mathrm{d}W}{\mathrm{d}R}+\frac{\lambda_E^3}{\lambda_p^{3/2}\mathcal{R}_f}+\frac{8}{3}\lambda_E^2\left(\frac{1}{G^3}-\frac{1}{G^9}\right)=0 \tag{B 1}$$

and

$$\frac{\mathrm{d}\Psi}{\mathrm{d}R}-\frac{\Psi}{R}+R\frac{\mathrm{d}^2\Psi}{\mathrm{d}R^2}+\frac{1}{2}\left(\frac{\mathrm{d}W}{\mathrm{d}R}\right)^2=0. \tag{B 2}$$

The boundary conditions become

$$W'(0)=0 \quad \text{and} \quad \lim_{R\to 0}[R\Psi'(R)-\nu\Psi(R)]=0 \tag{B 3}$$

at the origin and

$$W(\mathcal{R}_f)=0 \quad \text{and} \quad \mathcal{R}_f\Psi'(\mathcal{R}_f)-\nu\Psi(\mathcal{R}_f)=(1-\nu)\mathcal{R}_f\lambda_E^2/\lambda_T. \tag{B 4}$$

Fortunately, after this transformation, the system is explicitly reduced from five to four controlling parameters: λ_E, λ_T, λ_p and $\mathcal{R}_f$.

References

1. Ciavarella M, Joe J, Papangelo A, Barber J. 2019 The role of adhesion in contact mechanics. *J. R. Soc. Interface* **16**, 20180738. (doi:10.1098/rsif.2018.0738)
2. Lotfi M, Nejib M, Naceur M. 2013 Cell adhesion to biomaterials: concept of biocompatibility. In *Advances in biomaterials science and biomedical applications* (ed. R Pignatello), vol. 8, pp. 208–240. London, UK: IntechOpen.
3. Khalili AA, Ahmad MR. 2015 A review of cell adhesion studies for biomedical and biological applications. *Int. J. Mol. Sci.* **16**, 18 149–18 184. (doi:10.3390/ijms160818149)
4. Liu W, Xie R, Zhu J, Wu J, Hui J, Zheng X, Huo F, Fan D. 2022 A temperature responsive adhesive hydrogel for fabrication of flexible electronic sensors. *npj Flex. Electron.* **6**, 68. (doi:10.1038/s41528-022-00193-5)
5. He X *et al.* 2023 Adhesive tapes: from daily necessities to flexible smart electronics. *Appl. Phys. Rev.* **10**, 011305. (doi:10.1063/5.0107318)
6. Bradley R. 1932 LXXIX. The cohesive force between solid surfaces and the surface energy of solids. *Lond. Edinb. Dublin Philos. Mag. J. Sci.* **13**, 853–862. (doi:10.1080/14786449209461990)
7. Johnson KL, Kendall K, Roberts A. 1971 Surface energy and the contact of elastic solids. *Proc. R. Soc. Lond. A* **324**, 301–313. (doi:10.1098/rspa.1971.0141)
8. Derjaguin BV, Muller VM, Toporov YP. 1975 Effect of contact deformations on the adhesion of particles. *J. Colloid Interface Sci.* **53**, 314–326. (doi:10.1016/0021-9797(75)90018-1)
9. Tabor D. 1977 Surface forces and surface interactions. In *Plenary and invited lectures* (eds: Milton Kerker, Albert C. Zettlemoyer and Robert L. Rowell), pp. 3–14. Amsterdam, The Netherlands: Elsevier.
10. Maugis D. 1992 Adhesion of spheres: the JKR-DMT transition using a Dugdale model. *J. Colloid Interface Sci.* **150**, 243–269. (doi:10.1016/0021-9797(92)90285-T)
11. Greenwood J. 1997 Adhesion of elastic spheres. *Proc. R. Soc. Lond. A* **453**, 1277–1297. (doi:10.1098/rspa.1997.0070)
12. Johnson K, Greenwood J. 1997 An adhesion map for the contact of elastic spheres. *J. Colloid Interface Sci.* **192**, 326–333. (doi:10.1006/jcis.1997.4984)
13. Qian J, Lin J, Shi M. 2016 Combined dry and wet adhesion between a particle and an elastic substrate. *J. Colloid Interface Sci.* **483**, 321–333. (doi:10.1016/j.jcis.2016.08.049)
14. Butler MD, Vella D. 2022 Liquid bridge splitting enhances normal capillary adhesion and resistance to shear on rough surfaces. *J. Colloid Interface Sci.* **607**, 514–529. (doi:10.1016/j.jcis.2021.08.133)
15. Lu H, Qian J, Dai Z. 2025 Interplay of dry and capillary adhesion in elastic solids and structures. *J. Appl. Mech.* **92**, 111006. (doi:10.1115/1.4069116)
16. Wang Q, Papangelo A, Ciavarella M, Gao H, Li Q. 2025 Rapid detachment of a rigid sphere adhered to a viscoelastic substrate: an upper bound model incorporating Maugis parameter and preload effects. *J. Mech. Phys. Solids* **196**, 106028. (doi:10.1016/j.jmps.2025.106028)
17. Maghami A, Wang Q, Tricarico M, Ciavarella M, Li Q, Papangelo A. 2024 Bulk and fracture process zone contribution to the rate-dependent adhesion amplification in viscoelastic broad-band materials. *J. Mech. Phys. Solids* **193**, 105844. (doi:10.1016/j.jmps.2024.105844)
18. Shui L, Jia L, Li H, Guo J, Guo Z, Liu Y, Liu Z, Chen X. 2020 Rapid and continuous regulating adhesion strength by mechanical micro-vibration. *Nat. Commun.* **11**, 1583. (doi:10.1038/s41467-020-15447-x)
19. Tricarico M, Ciavarella M, Papangelo A. 2025 Enhancement of adhesion strength through microvibrations: modeling and experiments. *J. Mech. Phys. Solids* **196**, 106020. (doi:10.1016/j.jmps.2024.106020)
20. Dai Z. 2025 Jump of an atomic force microscopy probe towards an elastic substrate in a liquid environment. *J. Fluid Mech.* **1013**, A49. (doi:10.1017/jfm.2025.10290)
21. Salez T, Benzaquen M, Raphaël É. 2013 From adhesion to wetting of a soft particle. *Soft Matter* **9**, 10 699–10 704. (doi:10.1039/C3SM51780B)
22. Hui C-Y, Liu T, Salez T, Raphael E, Jagota A. 2015 Indentation of a rigid sphere into an elastic substrate with surface tension and adhesion. *Proc. R. Soc. A* **471**, 20140727. (doi:10.1098/rspa.2014.0727)
23. Long J, Wang G, Feng X-Q, Yu S. 2016 Effects of surface tension on the adhesive contact between a hard sphere and a soft substrate. *Int. J. Solids Struct.* **84**, 133–138. (doi:10.1016/j.ijsolstr.2016.01.021)

24. Zhu Y, Ni Y, Huang C, Yu J, Yao H, Zheng Z. 2025 Unified model for adhesive contact between solid surfaces at micro/nano-scale. *J. Mech. Phys. Solids* **196**, 106004. (doi:10.1016/j.jmps.2024.106004)
25. Lou L, Chen P, Liu H, Peng G, Peng J. 2025 Investigating the interfacial behavior of van der Waals heterostructures with nano-inclusions: molecular dynamics simulation and theoretical analysis. *Mech. Mater.* **212**, 105514. (doi:10.1016/j.mechmat.2025.105514)
26. Vella D. 2019 Buffering by buckling as a route for elastic deformation. *Nat. Rev. Phys.* **1**, 425–436. (doi:10.1038/s42254-019-0063-1)
27. Chen S, Wang G, Ciavarella M. 2026 Adhesive contact of elastic spherical shells: non-monotonic thickness dependence of pull-off force. *J. Mech. Phys. Solids* **206**, 106388. (doi:10.1016/j.jmps.2025.106388)
28. Zhao C, Wan K-T, Shan W. 2024 Progressive adhesion mechanics of elastomeric shells against a rigid substrate: from thin to thick. *Extr. Mech. Lett.* **68**, 102140. (doi:10.1016/j.eml.2024.102140)
29. Chandler TG, Vella D. 2020 Indentation of suspended two-dimensional solids: the signatures of geometrical and material nonlinearity. *J. Mech. Phys. Solids* **144**, 104109. (doi:10.1016/j.jmps.2020.104109)
30. Dai Z, Lu N. 2021 Poking and bulging of suspended thin sheets: slippage instabilities, and metrology. *J. Mech. Phys. Solids* **149**, 104320. (doi:10.1016/j.jmps.2021.104320)
31. Yu C *et al.* 2024 Stiffer is stickier: adhesion in elastic nanofilms. *Nano Lett.* **25**, 1876–1882. (doi:10.1021/acs.nanolett.4c05309)
32. Zhang S, Hou Y, Li S, Liu L, Zhang Z, Feng X-Q, Li Q. 2019 Tuning friction to a superlubric state via in-plane straining. *Proc. Natl Acad. Sci. USA* **116**, 24 452–24 456. (doi:10.1073/pnas.1907947116)
33. Li H, Yu C, Dai Z. 2024 Regimes in the axisymmetric stiction of thin elastic plates. *Int. J. Mech. Sci.* **284**, 109740. (doi:10.1016/j.ijmecsci.2024.109740)
34. Vella D, Davidovitch B. 2017 Indentation metrology of clamped ultra-thin elastic sheets. *Soft Matter* **13**, 2264–2278. (doi:10.1039/C6SM02451C)
35. Chen E, Dai Z. 2023 Axisymmetric peeling of thin elastic films: a perturbation solution. *J. Appl. Mech.* **90**, 101011. (doi:10.1115/1.4062831)
36. Dai Z. 2024 Analytical solutions for circular elastic membranes under pressure. *J. Appl. Mech.* **91**, 081002. (doi:10.1115/1.4065338)
37. Bico J, Reyssat É, Roman B. 2018 Elastocapillarity: when surface tension deforms elastic solids. *Annu. Rev. Fluid Mech.* **50**, 629–659. (doi:10.1146/annurev-fluid-122316-050130)
38. Dai Z, Liu L, Zhang Z. 2019 Strain engineering of 2D materials: issues and opportunities at the interface. *Adv. Mater.* **31**, 1805417. (doi:10.1002/adma.201805417)
39. Dai Z, Lu N, Liechti KM, Huang R. 2020 Mechanics at the interfaces of 2D materials: challenges and opportunities. *Curr. Opin. Solid State Mater. Sci.* **24**, 100837. (doi:10.1016/j.cossms.2020.100837)
40. Dong W, Dai Z, Liu L, Zhang Z. 2024 Toward clean 2D materials and devices: recent progress in transfer and cleaning methods. *Adv. Mater.* **36**, 2303014. (doi:10.1002/adma.202303014)
41. Akinwande D *et al.* 2017 A review on mechanics and mechanical properties of 2D materials—graphene and beyond. *Extr. Mech. Lett.* **13**, 42–77. (doi:10.1016/j.eml.2017.01.008)
42. Shanahan ME. 2000 Adhesion of a punch to a thin membrane. *C. R. Acad. Sci. IV Phys.* **1**, 517–522. (doi:10.1016/S1296-2147(00)00147-5)
43. Borodich FM, Galanov BA. 2016 Contact probing of stretched membranes and adhesive interactions: graphene and other two-dimensional materials. *Proc. R. Soc. A* **472**, 20160550. (doi:10.1098/rspa.2016.0550)
44. Zheng W, Dai Z. 2025 Universal pull-off force for separating a rigid sphere from a membrane. *J. Mech. Phys. Solids* **201**, 106163. (doi:10.1016/j.jmps.2025.106163)
45. Yuan W, Wang G. 2021 Adhesion between a rigid sphere and a stretched membrane using the Dugdale model. *Int. J. Solids Struct.* **208–209**, 214–220. (doi:10.1016/j.ijsolstr.2020.11.008)
46. Ru C. 2020 Adhesion of an elastic sphere on a tensioned membrane. *Math. Mech. Solids* **25**, 1534–1543. (doi:10.1177/1081286520909976)
47. Yuan W, Ding Y, Niu X, Wang G. 2024 Adhesion of a rigid sphere to a freestanding elastic membrane with pre-tension. *J. Appl. Mech.* **91**, 121008. (doi:10.1115/1.4066569)
48. Yu C, Zeng W, Kou Z, Wang W, Wang L, Li Q, Liu X, Dai Z. 2025 Transparency of graphene to solid–solid van der Waals interactions. *Phys. Rev. Lett.* **135**, 156202. (doi:10.1103/jgqz-gwlc)

49. Li H, Dai Z. 2025 Adhesion of elastic microbeams on thin deformable substrates. *Eng. Fract. Mech.* **313**, 110634. (doi:10.1016/j.engfracmech.2024.110634)
50. Chen E, Dai Z. 2025 Elastic sheets on Winkler foundations: indentation stiffness and nonlinearities. *Int. J. Solids Struct.* **315**, 113346. (doi:10.1016/j.ijsolstr.2025.113346)
51. Dai Z, Rao Y, Lu N. 2022 Two-dimensional crystals on adhesive substrates subjected to uniform transverse pressure. *Int. J. Solids Struct.* **257**, 111829. (doi:10.1016/j.ijsolstr.2022.111829)
52. Mansfield EH. 1989 *The bending and stretching of plates*. Cambridge: Cambridge University Press.
53. Yang X, Srivastava A, Long R. 2023 Adhesive contact of an inflated circular membrane with curved surfaces. *Int. J. Solids Struct.* **279**, 112371. (doi:10.1016/j.ijsolstr.2023.112371)
54. Cao J, Dai Z, Yu C, Wang W, Wei X, Wei Y. 2025 Fracture mechanics of 2D crystal blisters with irregular geometry. *Adv. Funct. Mater.*, e09438. (doi:10.1002/adfm.202509438)
55. Derjaguin VB. 1992 Theorie des anhaftens kleiner teilchen. *Prog. Surf. Sci.* **40**, 6–15. (doi:10.1016/0079-6816(92)90027-F)
56. Schmitz J, Benoit M, Gottschalk K-E. 2008 The viscoelasticity of membrane tethers and its importance for cell adhesion. *Biophys. J.* **95**, 1448–1459. (doi:10.1529/biophysj.107.124289)
57. Ying W, Yang F, Bick A, Oron G, Herzberg M. 2010 Extracellular polymeric substances (EPS) in a hybrid growth membrane bioreactor (HG-MBR): viscoelastic and adherence characteristics. *Environ. Sci. Technol.* **44**, 8636–8643. (doi:10.1021/es102309y)
58. Chang Z, Yang R, Wei Y. 2019 The linear-dependence of adhesion strength and adhesion range on temperature in soft membranes. *J. Mech. Phys. Solids* **132**, 103697. (doi:10.1016/j.jmps.2019.103697)
59. Polfus JM *et al.* 2021 Temperature-dependent adhesion in van der Waals heterostructures. *Adv. Mater. Interfaces* **8**, 2100838. (doi:10.1002/admi.202100838)
60. Aitken ZH, Huang R. 2010 Effects of mismatch strain and substrate surface corrugation on morphology of supported monolayer graphene. *J. Appl. Phys.* **107**, 123531. (doi:10.1063/1.3437642)
61. Ma Y, Li L, Smith A-S. 2024 Substrate topography regulating membrane adhesion mediated by receptor–ligand bonds. *Appl. Phys. Lett.* **125**, 153701. (doi:10.1063/5.0224078)